Volume 1
Number 3
May 2022
Pages 303–588

Sensors & Diagnostics

rsc.li/sensors

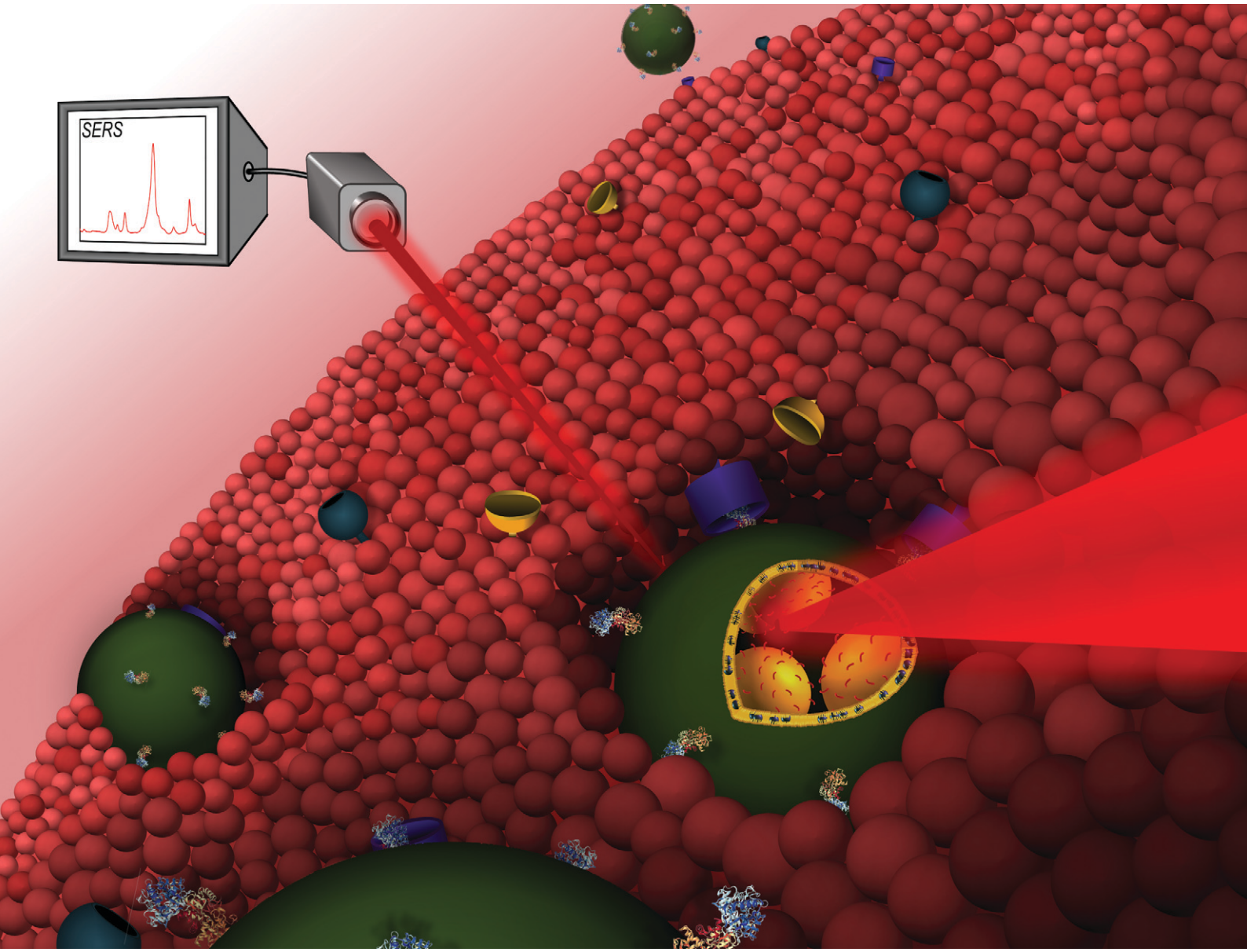

ISSN 2635-0998

ROYAL SOCIETY OF CHEMISTRY

PAPER
Georg Garnweitner *et al.*
All-in-one superparamagnetic and SERS-active niosomes for dual-targeted *in vitro* detection of breast cancer cells

Sensors & Diagnostics

PAPER

View Article Online
View Journal | View Issue

Cite this: *Sens. Diagn.*, 2022, **1**, 469

All-in-one superparamagnetic and SERS-active niosomes for dual-targeted *in vitro* detection of breast cancer cells†

Viktor Maurer,[ab] Ajmal Zarinwall,[ab] Zunhao Wang,[c] Stefan Wundrack,[c] Nicole Wundrack,[d] Didem Ag Seleci,[ab] Vivien Helm,[a] Daniil Otenko,[a] Claudia Frank,[c] Fred Schaper,[d] Rainer Stosch[c] and Georg Garnweitner *[ab]

In vitro and *in vivo* biosensing through surface-enhanced Raman scattering often suffer from signal contamination diminishing both the limit of detection and quantification. However, overcoming the lack of specificity requires excessive nanoparticle concentrations, which may lead to adverse side effects if applied to patients. In this study we propose encapsulation of iron oxide (Fe_xO_y) and gold (Au) nanoparticles (NPs) into the bilayer structure of transferrin-modified niosomes. This approach enables achieving greatly enhanced and contamination-free SERS-signals *in vitro* as well as a dual-targeting functionality towards MCF-7 breast cancer cells. An in-depth characterization of Fe_xO_yNPs- and AuNPs-loaded niosomes (AuNPs/Fe_xO_yNPs/NIO) after magnetic downstream processing reveals defined hybrid niosome structures, which show a long-term SERS-signal stability in various media such as MCF-7 cell culture medium. *In vitro* 2D-SERS imaging unveil a successful incorporation of a non-toxic dose of hybrid NPs into MCF-7 cells, which leads to strong and almost contamination-free SERS-signals. The measured signal-to-noise ratio of the *in vitro* signal exceeds the values required by DIN 32645 for the successful validation of a detection method. The hybrid niosomes can thus be considered a promising and efficient agent for the establishment and commercialization of a highly sensitive detection kit for monitoring cancerous tissue.

Received 29th January 2022,
Accepted 12th March 2022

DOI: 10.1039/d2sd00020b

rsc.li/sensors

1. Introduction

Nowadays, the survival rate for diseases such as breast cancer is significantly increased in the early stages of diagnosis and can be further improved by the availability of highly sensitive detection methods that allow an accurate monitoring of the disease progression.[1–3] Although widespread screening programs can crucially reduce the mortality rate, the current limitations in sensitivity and specificity of the existing imaging techniques explain an insufficient detection of smaller cancerous tissues, which results in complications and the need for invasive therapeutic procedures (*e.g.* resection of the breast) as well as disease recurrence.[4–7] Consequently, there is an increasingly pressing demand for accurate and cost-efficient cancer detection methods.

An emerging technique, the so called surface-enhanced Raman spectroscopy (SERS), provides outstandingly specific and sensitive detection of analytes such as biomarkers, cells and tissues, with accuracy reaching single-molecule level.[8–11] Using specially designed analytical nanoparticles (NPs) as SERS-tags, the target moieties can be selectively bound by the NPs and detected indirectly through the Raman signature of a Raman reporter molecule.[12–14] The use of plasmonic gold nanoparticles (AuNPs) has been particularly successful for this purpose. There are widely-used efficient and scalable bottom-up strategies to obtain highly uniform and spherical AuNPs, in particular wet chemistry methods or plant-based routes.[15–18] Whilst in principle nanoparticulate substances are also used in diverse therapies,[19–22] the outstanding performance of AuNPs in diagnostic procedures such as SERS as well as their biocompatibility allow versatile application in nanomedicine.

In contrast to the established bioimaging methods, SERS offers multiple advantages such as exceptionally high sensitivity, intrinsic molecular fingerprint information, resistance to photobleaching and -degradation as well as a

[a] *Institute for Particle Technology (iPAT), Technische Universität Braunschweig, Volkmaroder Str. 5, 38104 Braunschweig, Germany. E-mail: g.garnweitner@tu-braunschweig.de*
[b] *Center of Pharmaceutical Engineering (PVZ), Technische Universität Braunschweig, Franz-Liszt-Straße 35a, 38106 Braunschweig, Germany*
[c] *Physikalisch-Technische Bundesanstalt (PTB), Bundesallee 100, 38116 Braunschweig, Germany*
[d] *Institute for Biology (IBIO), Universität Magdeburg, Universitätsplatz 2, 39106 Magdeburg, Germany*

† Electronic supplementary information (ESI) available. See DOI: 10.1039/d2sd00020b

non-invasive long-term multiplex monitoring within various applications.[11,23–26] Despite proving its efficacy in several breast cancer-related *in vitro*, *in vivo* and *ex vivo* studies,[27–30] the clinical establishment of SERS still remains challenging due to several drawbacks: i) the slow uptake rate of bare SERS-tags, ii) uncertain biocompatibility, iii) interfering species (*e.g.* a protein corona) adsorbing onto the metallic surface after *in vitro*/*in vivo* administration. These drawbacks increase the noise signal and induce signal contamination.[31–35] Unspecific adsorption of biomolecules onto NPs in biological environments may lead to unforeseen physicochemical NP interactions followed by agglomeration and major signal fluctuations.[36–38] This results in a deteriorated detection limit which is detrimental for the successful validation of a diagnostic procedure according to the German standard method DIN 32645 and other international guidelines, thus hindering the establishment of a reliable detection method.[39,40]

To overcome these obstacles, an encapsulation of the prepared SERS-tags becomes progressively common. By using different inorganic (*e.g.* silica[41,42]) or organic (mostly liposomes/lipids,[43–45] polyethylene glycole (PEG)[46,47]) substances, single or multiple NPs can be incorporated in a shell of the respective substance. Especially an encapsulation of multiple functionalized plasmonic NPs into one carrier NP improves the biocompatibility, impedes the leaching of Raman-active molecules, reduces undesired NP–NP interactions and prevents signal contamination.[26,44,48] In addition, a shell-based spatial confinement of several NPs enhances the generation of plasmonic hot spots at interparticle gaps which yields in a drastic enhancement of SERS signal intensity.[49–51] Even though plasmonic NP-loaded liposomes are continuously being developed for implementation in biomedical research,[52–54] prevailing drawbacks still have to be addressed for a successful applicability. Most of the encapsulation procedures lack efficiency and require multiple post-synthetic purification steps to separate bare metallic NPs from the hybrid NPs, often leading to low yields and hence insufficient SERS signal intensities.[55,56] Moreover, the low physical and chemical stability of liposomes can result in a degradation of the structural integrity and leakage of the liposome structure throughout encapsulation and application.[54,57,58] Therefore, a novel method to assemble stable hybrids of encapsulated metal NPs is eminently needed.

To circumvent these case problems, another type of organic NPs, the so-called niosomes, can be utilized, which are also capable of entrapping optically active NPs to detect and visualize cancer.[59] Niosomes are vesicular carriers made of non-ionic surfactants forming a bilayer structure that allows the simultaneous encapsulation of hydrophilic and lipophilic compounds.[60–62] Due to the cheaper and commercially available surfactants, niosomes are more cost-efficient compared to other organic nanocarriers such as liposomes. Furthermore, niosomes have a chemically and physically more stable structure compared to liposomes which enables long storage times.[63] Additionally, their non-ionic nature makes them highly biocompatible and biodegradable.[64–66] The surface of niosomes can easily be modified with various biomarkers to address a targeting functionality.[67] These outstanding properties entitle niosomes a particular promising material for various future applications, with clinical trials already indicating a successful nanocarrier capability.[68–70]

Herein, we present a concurrent encapsulation of 5-thio-2-nitrobenzoic acid (TNB)-functionalized AuNPs and superparamagnetic iron-oxide nanoparticles (Fe_xO_yNPs) to accomplish the synthesis of the first niosomes with magnetic and SERS-active properties (Fig. 1). The main objectives were to protect the inorganic nanoparticles from external influences during biological application by encapsulating them into niosomes and thus to enable signal contamination-free SERS-imaging of breast cancer cells by means of the multifunctional properties of the resulting hybrid particle system. For this purpose, the hydrophilic AuNPs and hydrophobic Fe_xO_yNPs were synthesized, functionalized and characterized as described in previous publications.[71,72] PEG-maleimide-functionalized niosomes (NIO) and simultaneous encapsulation of the inorganic NPs were prepared using the thin-film hydration method similar to a recently published work,[59] followed by a magnetic purification procedure. Finally, the niosome surface was decorated with transferrin (Tf) to augment the uptake by malignant breast cancer cells *via* Tf-receptor-mediated endocytosis.[59,73,74] Throughout the hybrid niosome assembly, we investigated mainly two parameters to further enhance the resulting SERS-signal intensity: the addition of an ionic substance (HCl) to the AuNP solution before encapsulation and the overall AuNP mass fraction impact. The successful hybrid niosome (AuNPs/Fe_xO_yNPs/NIO/Tf) preparation was verified by investigating various particle properties using several methods such as i) dynamic light scattering (DLS), ii) SERS, iii) transmission electron microscopy (TEM), iv) UV/vis spectroscopy and iiv) zeta potential measurements. Moreover, by suspending the hybrid niosomes in different (complex biological) media, the long-term SERS-signal integrity and occurrence of possible signal contaminations was analysed over a period of 46 days. Ultimately, after verifying the biocompatibility within *in vitro* cytotoxicity studies, the hybrid niosomes were used for a 2D-SERS mapping of malignant MCF-7 breast cancer cells, hereby investigating the SERS-activity and signal integrity of the hybrid niosomes as well as confirming a successful detection according to national and international guidelines, such as the German standard method DIN 32645. Consequently, the hybrid niosomes revealed highly advantageous properties, combining excellent chemical stability, enhanced targeting functionality and remarkable SERS signal intensities, leading to great potential of the AuNPs/Fe_xO_yNPs/NIO/Tf as a sensitive SERS-based cancer detection platform technology.

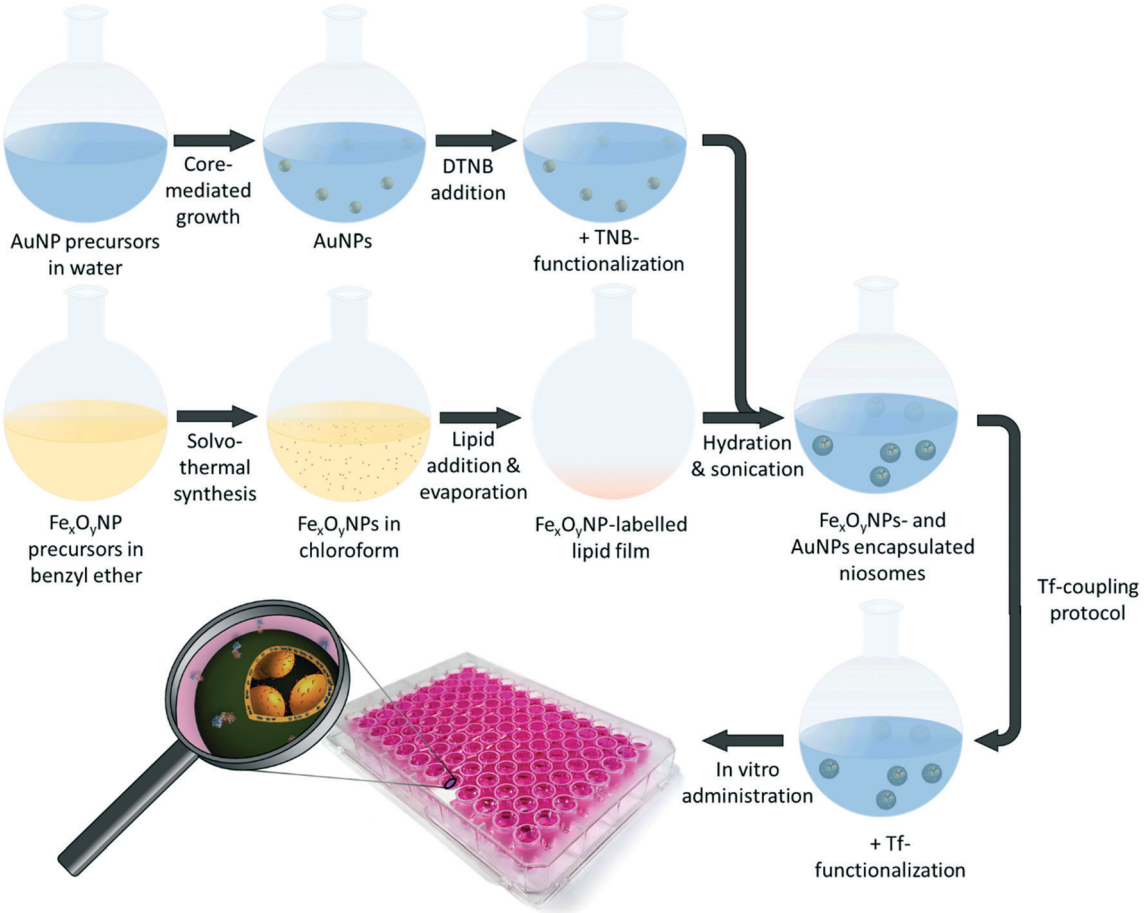

Fig. 1 Schematic depiction of the AuNPs/Fe_xO_yNPs/NIO/Tf formation and application.

2. Materials and methods

2.1 Chemicals and reagents

Benzyl ether (98%), cholesterol (≥99%), gold-(III) chloride (99%), 1,2-hexadecanediol (90%), hydrochloric acid (HCl, 37%), 4-(2-hydroxyethyl)-1-piperazineethanesulfonic acid (HEPES, ≥99.5%), 2-iminothiolane hydrochloride (Traut's reagent, ≥98%), insulin solution (human), iron-(III) acetylacetonate ($Fe(acac)_3$, ≥99%), non-essential amino acid solution (100×), oleic acid (90%), oleylamine (70%), phosphate buffered saline (PBS, tablet form), phosphotungstic acid (99.99%), polyethylene glycol 600 (PEG, techn. grade), sodium-(L) ascorbate (≥98%), sodium hydroxide (NaOH, ≥97%), sodium pyruvate solution, sorbitan monostearate (Span60), transferrin (Tf, ≥98%) and trypsin were obtained from Sigma-Aldrich Chemie GmbH (Taufkirchen, Germany). 1,2-distearoyl-*sn-glycero*-3-phosphoethanolamine-*N*-[maleimide(polyethylene-glycol)-2000] (DSPE-PEG(2000) maleimide) was provided by Avanti (Alabaster, USA). 5,5′-dithiobis-(2-nitrobenzoic acid) (DTNB, ≥99%) was acquired from AppliChem GmbH (Darmstadt, Germany). Fetal calf serum (FCS) was ordered from Biochrom GmbH (Berlin, Germany). Absolute ethanol (EtOH, 99.5%) was supplied by Fisher Scientific GmbH (Schwerte, Germany). Minimum essential medium (MEM) was purchased from Gibco life technologies (Carlsbad, USA). Ethylenediaminetetraacetic acid disodium salt dihydrate (EDTA, ≥99%) and sodium citrate dihydrate (≥99.95%) were ordered from Honeywell Fluka (Seelze, Germany). MCF-7 (breast adenocarcinoma) cell line was provided from German Collection of Microorganisms and Cell Cultures (DSMZ). All chemicals were used as received. Unless otherwise stated, ultrapure water was used. The HEPES buffer was prepared by dissolving HEPES powder (0.063 g) in ultrapure water (50 mL) and adjusting to a pH of 7.48–7.52 using a NaOH solution (0.1 mol L^{-1}). The PBS buffer (0.01 mol L^{-1}) for cell culture was obtained by dissolving one PBS tablet in ultrapure water (200 mL).

2.2 Synthesis of Fe_xO_yNPs

The solvothermal synthesis of the Fe_xO_yNPs and the particle properties were stated in our previous publication.[72] In summary, oleic acid (3 mmol) and oleylamine (3 mmol), $Fe(acac)_3$ (1 mmol) and 1,2-hexadecanediol (5 mmol) were added to a flask containing benzyl ether (10 mL) and heated to 100 °C for 30 min. Under nitrogen atmosphere, the mixture was first refluxed at 200 °C and afterwards at 265 °C

for 30 min each. The solution was cooled down to room temperature, followed by three washing steps with ethanol. After purification, the black precipitates were dispersed in chloroform. The notation Fe_xO_y is used in this report since the synthesized iron oxide NPs consist of both the magnetite Fe_3O_4 and maghemite γ-Fe_2O_3 phases.

2.3 Synthesis and TNB-functionalization of AuNPs

The synthesis procedure and a comprehensive characterization regarding the AuNP synthesis, TNB-functionalization and resulting particle properties (crystallinity, size, morphology *etc.*) was presented in our previous publication.[71] In short, the preparation of the core colloids was accomplished by refluxing a gold-(III) chloride solution (206 mL) while heating at 100 °C for 30 min and for another 15 min after addition of 50 mL citric acid solution. The synthesis of the final colloids was carried out by appending a sodium-(I) ascorbate solution (233 mL) and a gold-(III) chloride solution (233 mL) to a flask containing a core colloid solution (12 mL). Subsequently, after keeping the final solution at 30 °C for 1 h, the particles were purified *via* centrifuging and replacing the supernatant with HEPES buffer. By following this protocol, two different core colloids (AuNP 1 as well as AuNP 2) were synthesized. After specific ripening times, each core colloid was used to synthesize two final colloids (AuNP 1.1 and AuNP 1.2 as well as AuNP 2.1 and AuNP 2.2), respectively. The AuNP dispersions had a solid content of approx. 100 μg mL^{-1} (determined gravimetrically). The TNB-functionalization of AuNPs was performed by adding 10 μL of DTNB solution (7.9 mmol l^{-1}) per 50 μg mL^{-1} of AuNP dispersion. After a 30 min incubation, the particles were purified twice by centrifugation and replacing the supernatant with HEPES buffer.

2.4 Hybrid niosome synthesis *via* niosomal incorporation of Fe_xO_yNPs and AuNPs

The synthesis of PEG-maleimide-functionalized niosomes was based on the thin-film hydration method according to the protocol stated by Ag Seleci *et al.*[67] The incorporation of Fe_xO_yNPs to prepare Fe_xO_yNPs-loaded Niosomes (Fe_xO_yNPs/NIO) followed a slightly adapted procedure.[72] In short, Span60, cholesterol, and DSPE-PEG (2000) maleimide were dispersed in 1 mL chloroform (4.95 : 4.95 : 0.1 mmol L^{-1}). To this lipid mixture, 10 μL of Fe_xO_yNPs dispersed in chloroform (7.0 mg mL^{-1}) was added, followed by a rotary evaporation process for 2 h at 38 °C under decreased pressure (300 mbar). After successful formation of the lipid thin-film, 1 mL of TNB-functionalized AuNPs dispersed in water was added. In order to achieve lower repulsion forces between the AuNPs, HCl (2.5 μL) was put in some samples (which are referred to as AuNPs(HCl)). This was followed by sonication for 1 h at 65 °C. Then, utilizing a mini extruder set (Avanti Polar Lipids, USA), 20 extrusion cycles were performed, first using a 0.4 μm and then a 0.1 μm polycarbonate membrane to obtain the AuNPs/Fe_xO_yNPs/NIO hybrid NPs with an expected size of approx. 120 nm. To remove the excess HCl, a purification using a 12–14 kDa dialysis membrane was carried out for around 4 h. Finally, by attaching a 1.3 T permanent neodymium magnet to the samples for 16 h, the product containing the magnetically separated NPs (referred to as magn. sep.) and another sample with the remaining NPs in the supernatant (referred to as supernatant) was attained. For the preparation of a negative control consisting of a AuNP and Fe_xO_yNPs/NIO mixture (referred to as MIX AuNPs with Fe_xO_yNPs/NIO), ultrapure water (1 mL) was added to the thin-film containing flask to synthesize plain Fe_xO_yNPs/NIO, which was then sonicated and extruded as described before. Afterwards, the Fe_xO_yNPs/NIO solution (1 mL) was used to replace the decanted supernatant of precipitated TNB-functionalized AuNPs after the last purification step. Thereby, a mixture of AuNPs and Fe_xO_yNPs/NIO with the same AuNP mass content as the AuNPs/Fe_xO_yNPs/NIO sample was obtained, thus imitating a failed encapsulation process.

2.5 Finite-difference time domain simulations of E-field enhancement

The open-source software MEEP was utilized to perform two-dimensional finite-difference time-domain simulations (FDTD). Further explanation for the implemented FDTD algorithm and perfectly matched layers (PML) in MEEP can be found in the work of Oskooi *et al.*[75] A series of Lorentzian functions fitted to the measurement of Johnson *et al.* acted as the dielectric function of gold. The refractive indices of niosomes as well as Fe_xO_yNPs were set to 1.45 and 2.92, respectively, and water served as the background dielectric of the simulated structure.[76,77] For the light source, a continuous plane wave was utilized with the wavelength set to 633 nm. One single Yee cell was sized as 0.1 nm × 0.1 nm, whereas the remaining boundary conditions were PML. The E-field amplitude was output at all points in the area of interest. A calculation of the total E-field enhancement in one Yee cell was achieved by dividing the absolute square of the E-field amplitude with the squared amplitude of the incident E-field in the absence of the structure.

2.6 Preparation of Tf-conjugated hybrid niosomes

To prepare AuNPs/Fe_xO_yNPs/NIO/Tf, the conjugation of Tf to DSPE-PEG (2000) maleimide was performed analogously as reported previously.[59] Traut's reagent (50 nmol) and Tf (10 nmol) were suspended in HEPES EDTA buffer (500 μL) at pH 8.5 (30 mM HEPES and 0.1 mM EDTA). The thiolation of Tf was completed after incubating for 2 h at room temperature. In addition, using a size exclusion chromatography (30 kDa, Sephadex G50, Cytiva), the thiolated Tf was washed with HEPES (pH 6.5) and concentrated to a final volume of 200 μL. This was followed by an immediate application of hybrid niosome suspension (750 μL). A subsequent incubation for 24 h at 4 °C resulted in the formation of a thioether linkage[78] and the binding of the Tf-specific thiol groups to the maleimide moieties of the niosome PEG chains.

2.7 SERS-measurements in different media

The SERS-signal fluctuations of the AuNPs/Fe_xO_yNPs/NIO/Tf hybrid NPs and a negative control (plain TNB-functionalized AuNPs with the same AuNP mass content) in PBS (0.04 M), BSA (40 mg mL^{-1}) and MCF-7 cell culture medium with FCS (volumetric mixing ratio of NPs suspension : added medium was 2.5 : 1 for all samples) were examined over a period of 46 days. For a sufficient comparability of the samples, the initial SERS signal intensities for both the hybrid niosomes and negative control were normalized.

2.8 *In vitro* experiments

For the *in vitro* experiments, the cells were seeded on TPP® 96-well plates (Sarstedt, for cytotoxicity studies) or poly-L-lysine-(Sigma-Aldrich, for 2D-SERS measurements) coated cover glasses and cultured for 24 h in DMEM (Thermo Fisher Scientific, Waltham, MA, USA) supplemented with 10% FCS (Thermo Fisher Scientific), streptomycin, and penicillin (each 100 μg per ml, Thermo Fisher Scientific) at 37 °C in a water saturated atmosphere containing 5% CO_2. To assess the metabolic activity of MCF-7 cells after AuNPs/Fe_xO_yNPs/NIO/Tf administration, a CellTiter-Blue® cell viability assay was used to measure the reduction capacity of Resazurin (Promega Corp., Madison, WI, USA). 10^4 cells were seeded per well with 200 μL added cultivation medium and cultivated for 48 h. Afterwards, the cells were exposed with different concentrations of bare or Tf-loaded hybrid niosomes, incubated for 15 min by attaching a 1.3 T permanent neodymium magnet to achieve a magnetic guidance and subsequently incubated for 24 h. After diluting the CellTiter-Blue® reagent 1 : 10 with supplement-free MEM medium, 200 μl of the suspension was added to each well and incubated at 37 °C and 5% CO_2 for 4 h. A fluorescence spectrometer (GENios Microplate Reader, Tecan) was used to measure the fluorescence (530 nm excitation/590 nm emission). For the 2D-SERS measurements, the AuNPs/Fe_xO_yNPs/NIO/Tf were added in a non-toxic concentration (14 μl). The cells were incubated under the influence of a magnetic field (1.3 T permanent neodymium magnet) for 15 minutes. Subsequently the cells were grown in a water saturated atmosphere containing 5% CO_2 for 24 h at 37 °C. Afterwards cells were fixed with 4% paraformaldehyde (PFA, Carl Roth) at room temperature (21 °C) for 20 min and subsequently washed twice with PBS and mounted with Shandon Immu-Mount (9990402 Epredia) for following SERS measurements.

2.9 Characterization methods

The DLS and Zeta potential measurements were accomplished using a Zetasizer Nano ZS from Malvern Instruments. To minimize fluorescence, the samples were diluted by a factor of 10^4–10^5 and subsequently measured with a 173° backscattering set-up thrice. Using the Zetasizer Nano software, the data was evaluated utilizing the intensity distributions to assess the hydrodynamic diameters. The Zeta potentials were attained using a capillary zeta cuvette (DTS1070C, Malvern Panalytical Ltd). The pH-values of samples were acquired with the pH-meter Seven Compact from Mettler Toledo. To obtain SERS spectra, a LabRAM Aramis Raman microscope equipped with a 600 grooves per mm holographic grating and a HeNe excitation laser (633 nm) in combination with the LabSpec 5 Software from Horiba was used. Each sample was irradiated with an exposure time of 200 × 1 s with a spot size around 550 nm. Prior to each acquisition, the spectral line position was calibrated according to the recommendations given in the ASTM guideline using the polystyrene ring breathing mode at 1001.4 cm^{-1}.[79] The SERS-spectra of plain AuNP solutions (in section 3.1) were attained after adjusting their OD to 1 and adding HCl (4 μL, 1 M) to 250 μL of AuNP solution. For the 2D-SERS mappings, a 20× objective lens was used with an average image acquisition time of approx. 8 h. UV/Vis spectra were acquired using a LAMBDA 1050 dual-beam photometer from Perkin Elmer. The measurement was carried out in a Quartz Suprasil semi-micro cuvette (layer thickness 1.0 cm) from Hellma Analytics. TEM images were taken with a Tecnai G2 F20 TMP from FEI at 200 kV. For sample preparation, 20 μl of the solution were mixed with a staining solution (10 μl) containing 2% aqueous phosphotungstic acid and applied onto a carbon film on a 3.05 mm woven copper net with 300 mesh from Plano GmbH. Particle sizes were determined by measuring 50 nanoparticles, using the ImageJ software (version 1.42q).

3. Results and discussion

3.1 Raman properties of the AuNPs

In general, a reproducible application of SERS can only be realised by plasmonic nanoparticles with homogeneous particle properties. Therefore, an in-depth characterization of the AuNP plasmonic properties is essential. To investigate the influence of ripening time and core colloid size on the SERS activity, the synthesis of four final AuNP solutions was carried out using two core colloids with a size difference of 4.5 nm (Fig. S1a†) after specific core colloid ripening times (10 and 42 days as well as 1 and 51 days, respectively). Representative TEM images of the four synthesized AuNP samples confirm equally sized particles of approx. 38–40 nm with no morphological variances (Fig. 2a). All TNB-functionalized AuNPs were measured analogously *via* SERS by adding HCl as stated in section 4 (characterization methods) to characterize the Raman enhancing ability. Fig. 2b illustrates a typical Raman spectrum of the TNB-functionalized AuNPs with the characteristic Raman peaks at 852 cm^{-1} (nitro scissoring vibration), 1067 cm^{-1} (succinimidyl stretch overlapping with aromatic ring modes), 1341 cm^{-1} (symmetric stretch of the nitro group) and 1559 cm^{-1} (aromatic ring stretching modes).[80] For further SERS intensity comparisons between the obtained TNB spectra, the intensity of the dominating nitro group stretch signal mode at 1341

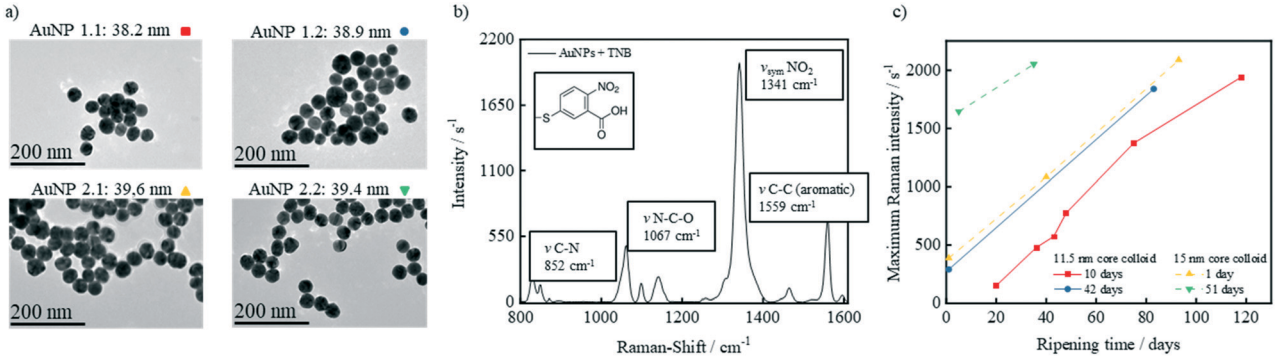

Fig. 2 a) Representative TEM images of the four ascorbate-stabilized AuNPs samples; b) SERS spectrum with four characteristic vibrational assignments of TNB-functionalized AuNPs and c) maximum Raman intensity (=intensity of the nitric group stretch) measured throughout the final colloid ripening time of the four AuNP solutions shown in a), which were synthesized using differently sized core colloids (11.5 nm and 15.0 nm) after respective core colloid ripening times (10 and 42 days as well as 1 and 51 days).

cm^{-1} was used and referred to as the "maximum Raman intensity".

After different final colloid ripening times (up to 120 days), SERS-spectra were measured (Fig. 2c). For all AuNPs, a longer final colloid ripening time results in a higher maximum Raman intensity. This is probably based on the growth of AuNPs due to Ostwald ripening and thus, the presence of larger SERS scattering centres.[81] By comparing the AuNPs synthesized from the core colloids with the same size but different core colloid ripening times, a superior

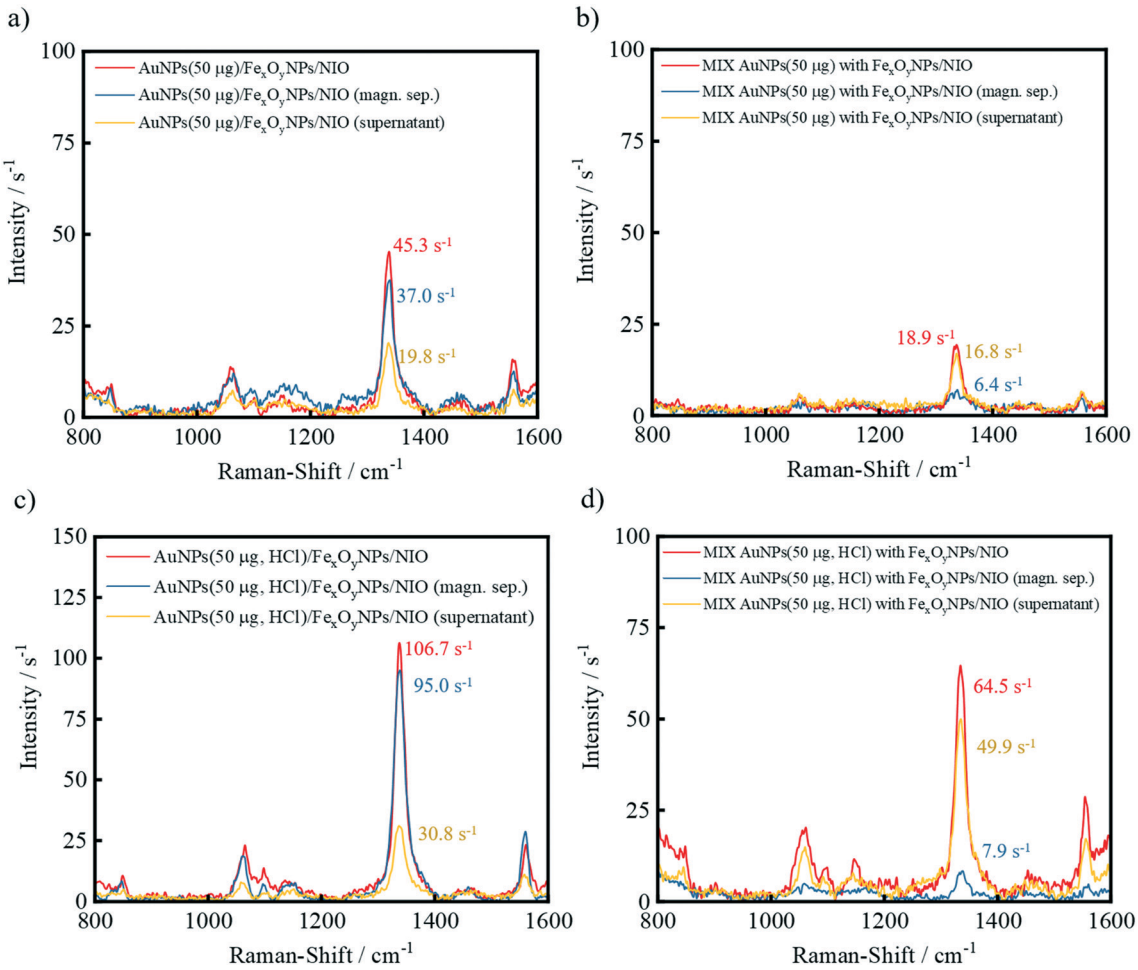

Fig. 3 SERS spectra measured before and after magnetic separation obtained from the a) hybrid niosomes, b) negative control, c) hybrid niosomes with previously added HCl and d) negative control with previously added HCl.

maximum Raman intensity after identical final colloid ripening times as a consequence of a longer core colloid ripening time becomes obvious. Apart from the ripening times, the core colloid particle size shows strong impact on the Raman intensity: AuNPs with a similar core colloid ripening time (AuNP 1.1 and AuNP 2.1, AuNP 1.2 and AuNP 2.2) still differ in their maximum Raman intensity at identical final colloid ripening times. The fact that larger core colloids lead to increased Raman intensities can be attributed to the high crystallinity of the core particles, which predominantly contribute to the Raman enhancing effect in contrast to the partly amorphous AuNP shell.[71] Since the limit of detection (LOD) and limit of quantification (LOQ) crucially depend on the signal-to-noise ratio, these results emphasise that larger core colloids with longer core and final colloid ripening times are essential to achieve higher Raman intensities and consequently to gain more sensitivity. After different periods, all AuNPs reached a maximum Raman intensity of approx. 2200 s^{-1} and were used subsequently for the following experiments.

3.2 Synthesis of magnetic and SERS-active niosomes

The concurrent encapsulation of the TNB-functionalized AuNPs (in the presence or absence of HCl while AuNP preparation) and Fe_xO_yNPs was performed following the procedures shown in Fig. 1. In the thin-film hydration method, evaporation of chloroform initially leads to the formation of a multilayer lipid film consisting of the basic niosomal components. In the course of the layer formation, the Fe_xO_yNPs are deposited between the fatty acid residues of the niosomal components and thus intercalate within the individual layers. Rehydration causes the lipid cake to swell, whereby the aqueous medium and the dispersed gold nanoparticles permeate between the bilayers, thus forming large multilamellar AuNP/Fe_xO_yNPs/NIO.

To verify the Raman enhancing ability of the encapsulated AuNPs as well as the successful magnetic separation process, SERS-spectra were recorded before magnetic purification (red spectra) and after removing the supernatant (yellow spectra) from the magnetically separated product (blue spectra) (Fig. 3).

For the hybrid niosome samples, a distinct Raman intensity after the magnetic separation procedure was measured, indicating the presence of TNB-functionalized AuNPs. Comparing the sample with the respective negative control (blue spectra Fig. 1a with b), the difference of 30.6 s^{-1} (37.0 s^{-1} − 6.4 s^{-1}) implies successfully encapsulated and magnetically separated TNB-functionalized AuNPs. With previously included HCl, a higher intensity difference of 87.1 s^{-1} (95.0 s^{-1} − 7.9 s^{-1}) for the hybrid niosome sample and negative control (blue spectra Fig. 1c with d) was obtained. In contrast to the samples without HCl, the substantially higher Raman intensity of the HCl-treated AuNP sample implicates the successful encapsulation of more AuNPs due to the acid-induced reduction of the AuNP surface charge, hence lowering the repulsion forces and distances from each other throughout the encapsulation process.

Apart from the preceding addition of an ionic substance (*e.g.* HCl), the Raman intensity can be increased by using higher AuNP amounts in the encapsulation procedure (Fig. 4a). While AuNP amounts below 20 μg result in almost negligible Raman intensities, raised amounts (40 μg, 50 μg and 80 μg) lead to a sharp intensity increase. This disproportionate Raman intensity surge can be attributed to an enlarged amount of encapsulated AuNPs per niosome and thus a larger number of generated interparticle plasmonic hotspots generated. If the amount of AuNPs is further incremented (for example to 200 μg), only a smaller rise in signal intensity was measured, suggesting a saturation of niosomes with encapsulated gold nanoparticles thus indicating that the average number of AuNP per niosome can hardly be increased. Comparing 50 μg and 80 μg hybrid

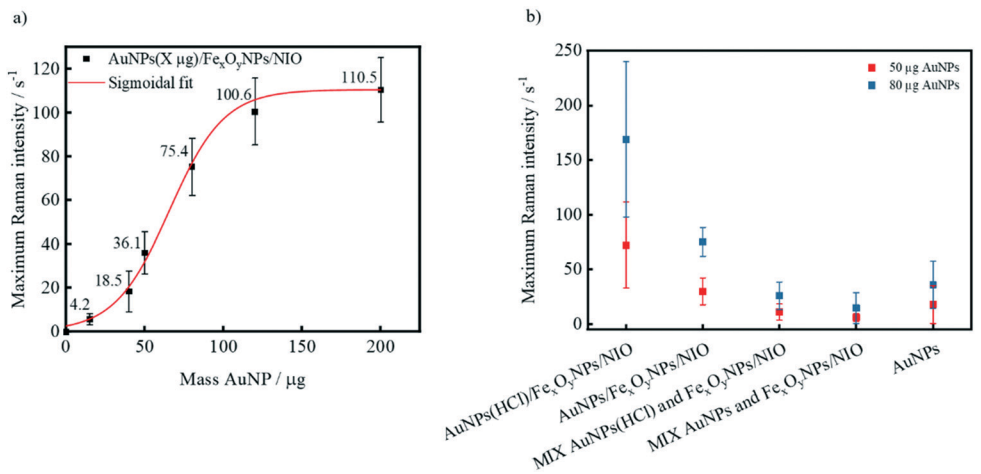

Fig. 4 Measured maximum Raman intensities of a) hybrid niosomes after addition of different AuNP mass fractions and b) hybrid niosomes and negative controls (with a utilized AuNP mass of both 50 μg and 80 μg) in dependence of a previous HCl addition.

niosomes samples with added HCl (Fig. 4b), the 80 μg sample shows a maximum Raman intensity either due to an amplified amount of encapsulated AuNPs, lower repulsion forces between incorporated AuNPs or both. When using 80 μg AuNPs instead of 50 μg, the difference between the mean intensities of the respective AuNP(HCl)/Fe_xO_yNPs/NIO to the respective negative control (MIX AuNP(HCl) with Fe_xO_y/NIO) grows significantly. This implies that in contrast to the lower amount, the addition of 80 μg AuNPs before encapsulation process leads to an amplified maximum Raman intensity of the resulting hybrid niosomes, whereas the amount of AuNPs that remains in the solution after magnetic separation and still generates low Raman signals is almost identical. Furthermore, even after removing a significant amount of AuNPs in the magnetic separation procedure, the AuNP (80 μg, HCl)/Fe_xO_yNPs/NIO surpasses the maximum Raman intensity of a plain 80 μg AuNP dispersion, indicating a successful SERS-active niosome synthesis. Since the maximum Raman intensity of hybrid niosome samples with less than 80 μg AuNPs is quite low and the use of AuNP amounts above 80 μg often resulted in particle agglomeration (data not shown), for all further experiments, unless otherwise stated, an amount of 80 μg AuNPs with previously added HCl was utilized for the hybrid niosomes preparation (in the following simply referred to as AuNPs/Fe_xO_yNPs/NIO).

Repeated measurements of the hybrid niosomes SERS-activity during a period of 46 days reveal hardly any SERS-signal intensity fluctuations over the first 11 days (Fig. S1b†). The increase in signal intensity by approx. 37% within the following 35 days is probably due to a continuous agglomeration of the entrapped AuNPs. Stable SERS-activity is a good indication for a long-term stability of the hybrid niosome suspension.

Additionally, TEM images were recorded to display the successful encapsulation of the inorganic NPs (Fig. 5). A representative TEM image of TNB-functionalized AuNPs that exhibit a strong contrast to the background can be seen in Fig. 5a. If only AuNPs are encapsulated into niosomes, the edges of the AuNPs are surrounded by a greyish layer, which can be attributed to the disintegrated organic niosome shell (Fig. 5b). An encapsulation of Fe_xO_yNPs into niosomes leads to the occurrence of smaller and less contrasting Fe_xO_yNP

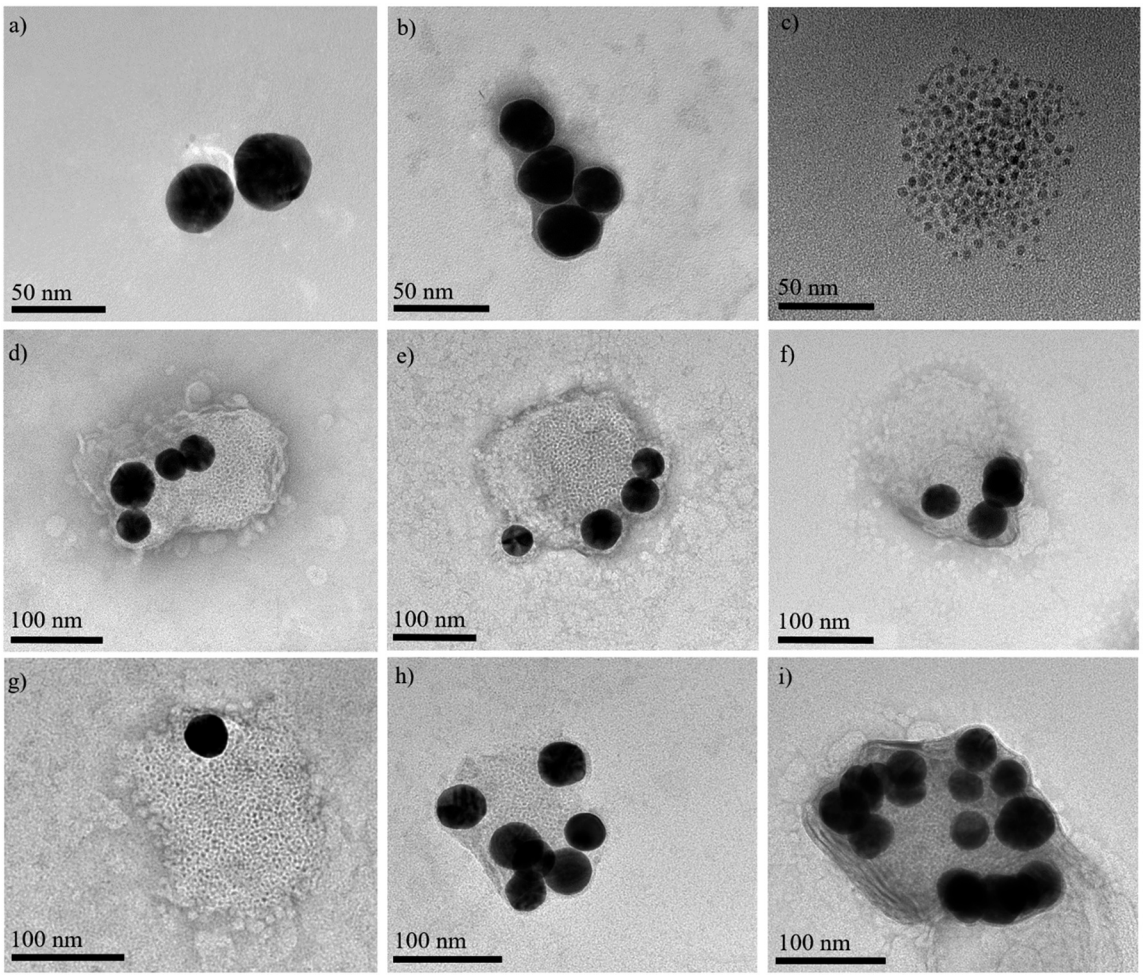

Fig. 5 Representative TEM images of a) TNB-functionalized AuNPs, b) AuNP-loaded niosomes, c) Fe_xO_yNPs/NIO, d)–i) AuNPs/Fe_xO_yNPs/NIO hybrid niosomes.

clusters with a diameter of around 100 nm that can be related to niosomes (Fig. 5c). After co-encapsulation of AuNPs and Fe_xO_yNPs, the formation of defined AuNPs/Fe_xO_yNPs/NIO hybrid NPs can be clearly recognized in the TEM images (Fig. 5d–i). Next to the bigger high- contrast AuNPs, smaller low-contrast Fe_xO_yNPs are located, with both NP types being surrounded by an organic shell structure, thereby forming the hybrid niosome. Most frequently, four AuNPs were found to be incorporated per niosome (Fig. 5d–f) whereas the observed number varies between one and up to 15 AuNPs (Fig. 5g–i). It should be noted that the size of the hybrid niosomes in the pictures is in the range of 150–250 nm, which can be attributed to the destruction of the spherical 3D structure due to sample drying and the electron beam focus, leading to the formation of a planar and therefore larger quasi-2D layer.

To get a deeper insight into the SERS activity of AuNPs/Fe_xO_yNPs/NIO, the resulting electromagnetic field (E-field) enhancement, which is created by the electromagnetic radiation of metallic NPs, was calculated using finite-difference time-domain simulations (FDTD) simulations. For the AuNPs/Fe_xO_yNPs/NIO, TNB as the Raman-active compound is immobilized onto the AuNPs, which are encapsulated in a water-filled, spherical niosome bilayer (Fig. 6a). The FDTD simulation demonstrated that the Fe_xO_yNPs-containing niosome layer does not significantly influence the resulting E-field on amplification the surface of the AuNPs at various distances (Fig. 6b). Furthermore, the highest enhancement of the E-field on the inside of the niosome layer is several orders of magnitude lower than between two AuNP surfaces, even at a maximum interparticle distance (approx. 10 nm for two 40 nm sized AuNPs inside a 90 nm niosome core) (Fig. 6c and d). This confirms that, as already demonstrated in Fig. 3 experimentally, the measured SERS-spectra of the AuNPs/Fe_xO_yNPs/NIO are almost exclusively composed of the specific vibrations of the TNB and do not exhibit any structural artefacts of the Fe_xO_yNPs/NIO. Simulating the E-field enhancement of the AuNPs/Fe_xO_yNPs/NIO illustrated in the TEM-image of Fig. 5d, a congruent result was obtained (Fig. 6e) as well as for AuNPs/NIO in Fig. 5b (Fig. S3†).

Recorded UV/vis-spectra illustrate an overall reduction in extinction (especially the AuNP-specific maximum) for the hybrid niosomes and negative controls after magnetic separation, indicating a lower concentration of NPs in the resulting suspensions (Fig. 7a). Since the majority of the AuNPs in the negative control sample is removed after magnetic purification, a AuNP-specific maximum is hardly visible. The large optical density (OD) discrepancy of the magnetically purified dispersions can thus be attributed to the successful AuNP encapsulation and hence raised mass fraction in the solution. Although the AuNPs/Fe_xO_yNPs/NIO sample after magnetic separation contain a lower AuNP amount than the supernatant sample (Fig. S4a and b†), Fig. 3 showed that the exhibited SERS-intensity after magnetic separation is several times higher than the resulting SERS-intensity of the supernatant, which is a clear evidence for encapsulation and thereby induced SERS-activity.

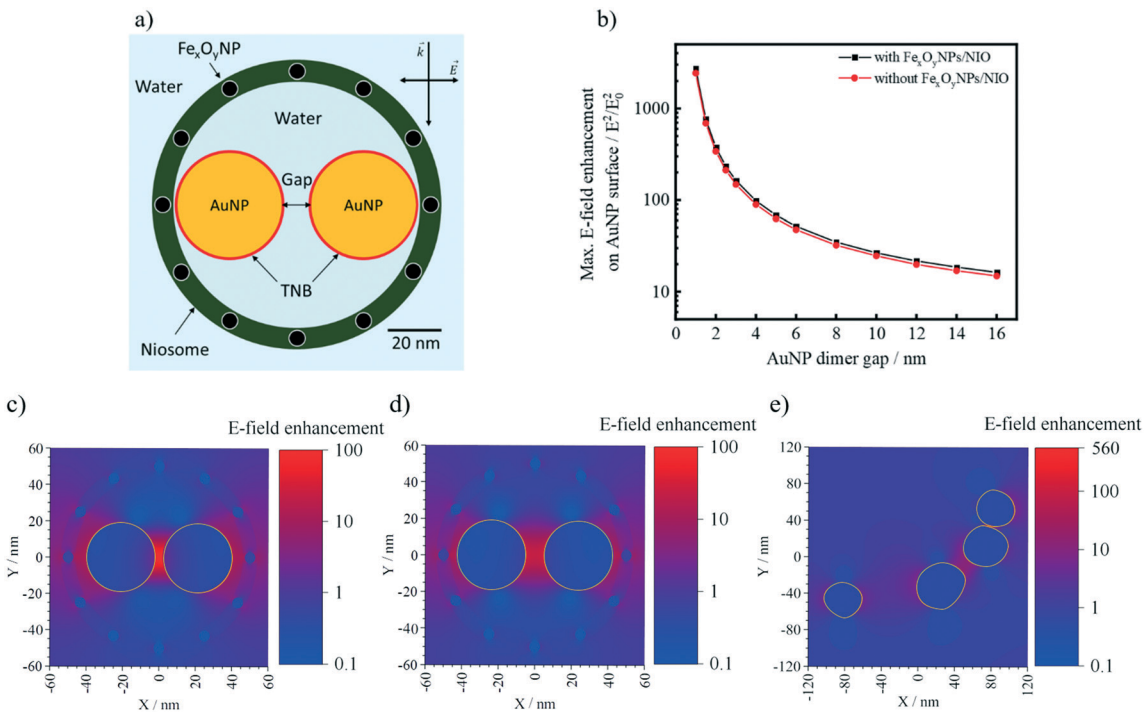

Fig. 6 a) Schematic representation of AuNPs/Fe_xO_yNPs/NIO utilized for the FDTD simulations; b) calculated maximum E-field enhancement on the AuNP surface for AuNPs/Fe_xO_yNPs/NIO and AuNPs/NIO with variant interparticle gap; FDTD simulated E-field enhancement of AuNPs/Fe_xO_yNPs/NIO with a AuNP (encircled in gold) gap distance of c) 4 nm, d) 10 nm, and e) for the AuNPs/Fe_xO_yNPs/NIO from the TEM image in Fig. 5e.

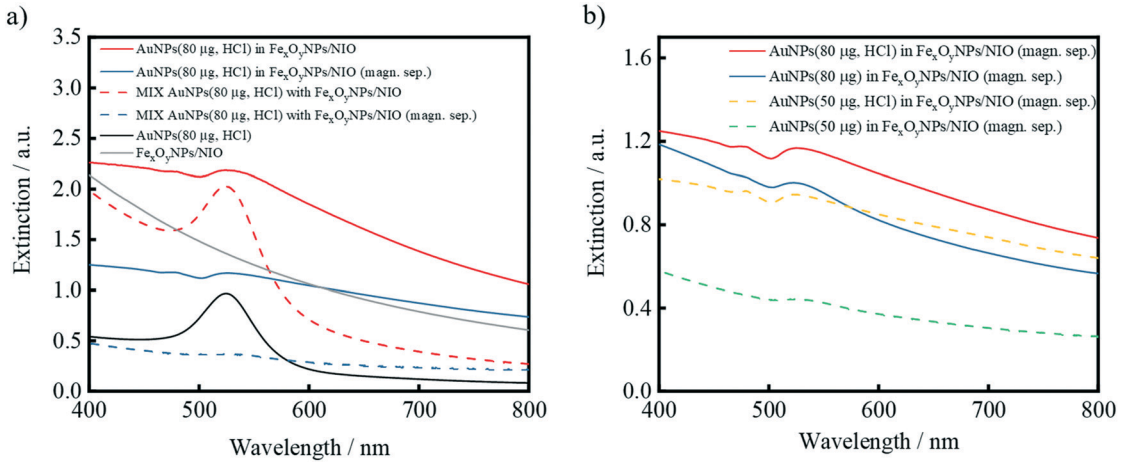

Fig. 7 Measured UV/vis spectra a) before and after magnetic purification obtained from hybrid niosomes and negative controls and b) hybrid niosomes with different AuNPs mass fractions as well as with and without previously added HCl.

Furthermore, the spectra of AuNPs/Fe$_x$O$_y$NPs/NIO samples with different AuNP mass fractions were compared (Fig. 7b). Regardless of a previous HCl addition, a higher OD and thus an increased number of encapsulated AuNPs is obtained after induction of a higher AuNP mass fraction within the encapsulation procedure. This relation is in good agreement with the SERS results displayed in Fig. 4. A further analogy to the results of the SERS measurements becomes comprehensible when comparing UV/vis spectra of the same AuNP mass: adding HCl before the encapsulation process also leads to an elevated OD suggesting a more efficient encapsulation of AuNPs. Moreover, compared to the samples without included HCl, the spectra of the HCl-treated AuNP samples reveal a more steadily decreasing curve profile after the maximum at approx. 526 nm, which becomes clearer when comparing the first derivative of the curves: after the minimum at around 560 nm, the slope of the samples without added HCl increases faster than the slope of the samples with HCl-treated AuNP, which even display smaller minima at approx. 730 nm (Fig. S4c†). This can be attributed to the HCl-induced proximity among AuNPs within the hybrid structure and the resulting coupling of their surface plasmon resonance.[82,83]

DLS measurements confirm that the average particle size of the hybrid niosomes and negative control after magnetic separation is approximately 120 nm which predominantly indicates the presence of niosomes (Fig. 8a). This hydrodynamic diameter is in the size range of bare Fe$_x$O$_y$NPs/NIO, which is expected to ensure a flawless uptake by cancer cells *via* receptor-mediated endocytosis.[84–86]

Furthermore, it is shown that the Zeta potential of the AuNPs/Fe$_x$O$_y$NPs/NIO and the negative control are almost equal after magnetic separation and correspond to the value of Fe$_x$O$_y$NPs/NIO, thus proving a successful magnetic separation procedure (Fig. 8b). Moreover, the final zeta potential of 35 mV indicates an electrostatically well-stabilized suspension. The zeta potential of the supernatants resemble the AuNP-specific zeta potential due to the abundance of free AuNPs (Fig. S5a and b†).

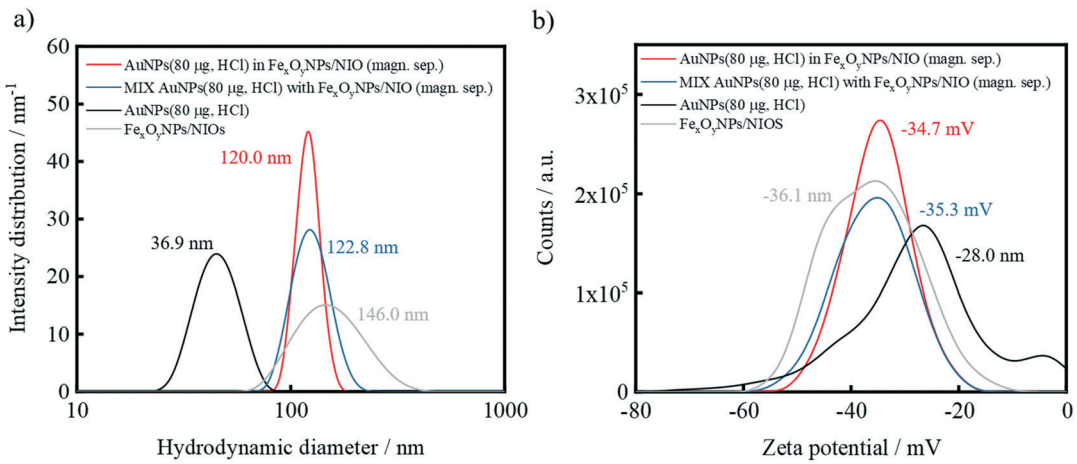

Fig. 8 a) DLS measurements and b) zeta potentials of the hybrid niosomes and negative control.

3.3 Administration of hybrid niosomes to complex media

After the successful synthesis, magnetic purification and characterization of the AuNPs/Fe_xO_yNPs/NIO, an investigation of the niosomal shielding effect on the SERS-signal integrity against external influences (*e.g.* high osmotic pressure, biological molecules, acidic environment *etc.*) that usually affect NPs after administration in organisms was realized. For this purpose, three different media were prepared: phosphate-buffered saline (PBS), a saturated bovine serum albumin (BSA) suspension and the cell culture medium (CCM) used to cultivate MCF-7 breast cancer cells. After the addition of the respective medium, there is initially a slight reduction in the SERS signal intensity ("0 days"), which is mainly due to the dilution of the respective sample. If PBS is added to plain TNB-functionalized AuNPs, a strong increase in the SERS-signal intensity is initially recorded due to a reduction of the repulsive forces between the AuNPs, thus resulting in an exalted generation of interparticle SERS-hotspots (Fig. 9a). This is followed by a rapid decrease within the first hours, which finally leads to a complete and persistent loss of SERS-signal due to the formation of large particle agglomerates and subsequent sedimentation. The hybrid niosomes, on the other hand, show no major fluctuations as a result of the niosomal shielding, with a decrease in signal intensity of approximately 35% only after an extended storage. This is probably caused by a partial loss of the structural integrity of some niosomes due to the high osmotic pressure of the PBS suspension. Nevertheless, qualitative identification of the symmetrical stretching vibrations of the nitro group is still clearly possible even after 46 days (Fig. 9b). After addition of the BSA solution to plain AuNPs, a steady decrease in signal intensity was observed, followed by a stable signal intensity until the 46th day (Fig. 9a). In contrast, the signal fluctuations of the hybrid niosomes are again negligible throughout the entire measurement period, and an enhanced SERS signal intensity with only a small proportion of signal contamination is seen in the spectrum at longer storage times (Fig. 9c), mainly attributed to the high concentration and consequently increased Raman-scattering of BSA. The change in the signal intensity of the hybrid niosomes in CCM and the underlying causes are rather analogous to the case of PBS due to a similarly high osmotic pressure. The SERS signal intensity of the plain AuNPs in CCM decreases sharply within the first days and remains below the detection limit for the further measurements. The reason for this is a strong signal contamination by the components of CCM, which are adsorbed onto the AuNP surface and thus do not allow a clear identification of the symmetrical stretching oscillation of the nitro group (Fig. 9d).

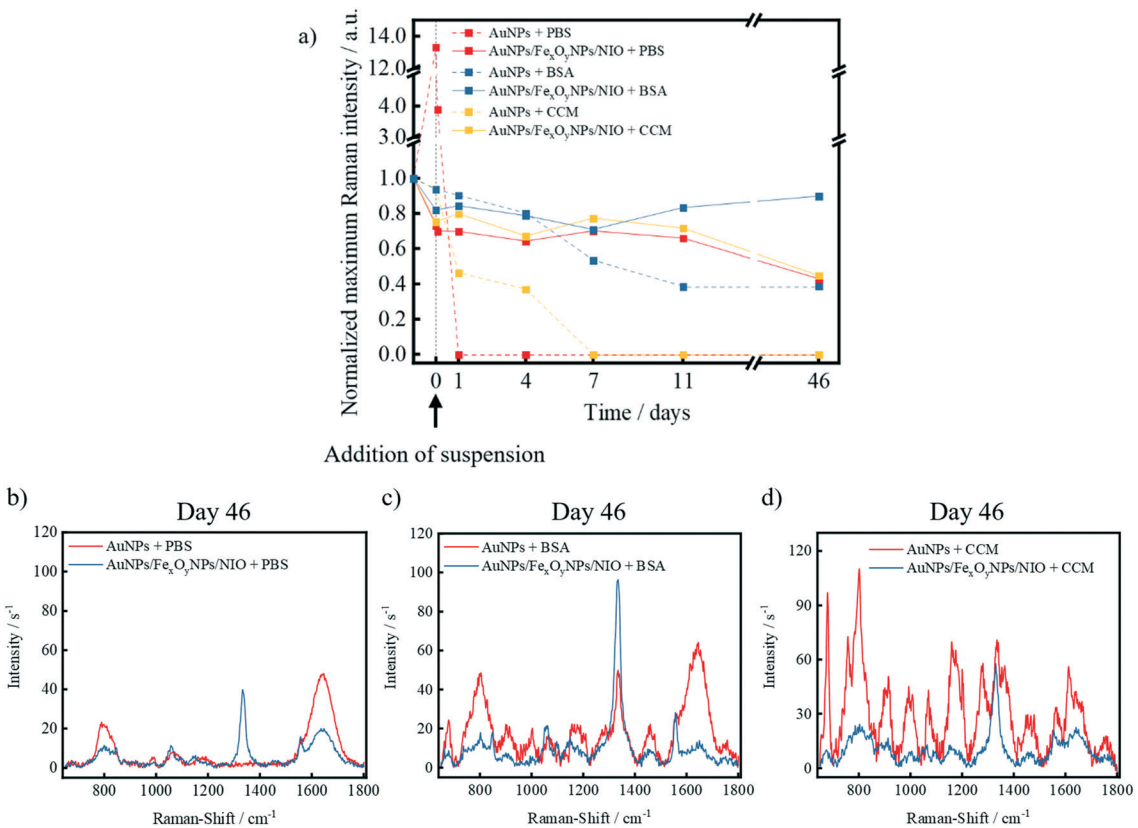

Fig. 9 a) SERS-signal intensity variations of AuNPs/Fe_xO_yNPs/NIO and plain TNB-functionalized AuNPs throughout 46 days after addition of the respective medium (PBS, BSA or CCM); b–d) SERS-spectra of the hybrid niosomes and plain TNB-functionalized AuNPs on the 46th day after addition of PBS, BSA and CCM.

To investigate possible signal variations due to an acidic environment (as present in most cancer cells), HCl (1 M, 4 μL) was added post-synthetically to hybrid niosomes and negative control dispersions (Fig. S2a†). In contrast to the plain AuNP solution, no significant Raman intensity changes occurred in any of the niosome-containing samples, indicating the prevention of different interparticle hotspot generation. Furthermore, encapsulated AuNPs are shielded by the niosomes against the surrounding acid, whereas the niosomes in the MIX negative control sample may sterically prevent a spatial approximation of the AuNPs. Further pH measurements confirm that these results are not based on a pH-buffering ability of the niosomes since the acid addition results in a pH decrease to 2.0–2.2 for all samples (Fig. S2b†). Moreover, the neutral pH-values of the AuNPs(HCl)/Fe_xO_yNPs/NIO samples before applying the acid prove that the initially included HCl has been removed in the dialysis step, thus indicating the possibility of further *in vitro* experiments without acid-based side effects.

These results suggest that the niosomes act as a protective layer against a wide range of different molecules and pH-shifts found in biological environments, thus serve to maintaining the SERS-activity over a long storage period. In particular, the results in CCM show that after administration of the particles *in vitro*, no signal contamination by the cultivation medium itself and therefore no influence of the medium on cell imaging can be expected.

3.4 *In vitro* experiments

Since intracellular SERS detection vitally depends on the efficient internalization of the SERS nanoprobes, it is highly important to develop methods that can effectively deliver the SERS-active NPs into the cell. Considering that a disordered iron metabolism is a hallmark of cancer cells, the Tf-receptor is commonly used as a prominent marker of cancer cells and also identified as a therapeutic target.[87] Remarkably, Tf-receptor 1 (CD71),[88,89] but also other iron-regulating and -regulated proteins such as transcription factors[90] are overexpressed in human breast cancer cells. Therefore, apart from a successful iron-oxide based magnetic targeting with an external magnetic field,[72,91] a second, cell-specific targeting functionality was necessary. As the niosomes are to be used to label breast cancer cells, the Tf-receptor system is a preferable route for internalization of niosomes. Thus, Tf was coupled to the maleimide groups of the hybrid niosomes. The successful Tf-functionalization of the hybrid niosomes was investigated using zeta potential measurements, which clearly showed a decrease in the absolute value of the zeta potential due to the coupling of positively charged Tf (Fig. S6†) similar to the results reported in other works.[59,92]

Since the synthesized hybrid niosomes will be primarily used for the detection of living breast cancer cells, particularly uncontrolled necrotic signal cascades should be avoided. Hence, cytotoxicity studies were carried out using MCF-7 breast cancer cells (Fig. 10). From the results of our experiments, we conclude that a hybrid niosomes dispersion volume of at least 14 μL per 10 k MCF-7 cells leads to no significant reduction in viability and therefore can be assumed as a safe volume for *in vitro* administration. However, for hybrid niosome volumes larger than 14 μL, surface modification with Tf leads to slightly reduced viability. This interference can be attributed to an increased uptake of the functionalized hybrid niosomes due to a successful Tf-receptor-mediated endocytosis.

In vitro 2D SERS images clearly demonstrate that the dyadic targeting composed of a magnetic manipulation as well as Tf-based endocytosis resulted in the accumulation of AuNPs/Fe_xO_yNPs/NIO in MCF-7 cells after 24 hours of incubation (Fig. 11). Strong localized TNB-signals were detected, possibly indicating an accumulation in specific cell compartments, as well as a non-specific accretion throughout the cytosol of the cell. The oscillation of the TNB nitro group in the *in vitro* SERS-spectra is located at approx. 1341 cm^{-1} as in the TNB-reference spectra. Apart from a minor background noise, no signal contamination can be detected, which indicates the structural integrity of the hybrid niosomes. The calculated signal-to-noise ratios (SNR) are always clearly above the prescribed SNR minimum of 9.0 according to national and international guidelines, such as DIN 32645. In particular, the highest occurring SNR in the center of each region of interest is 3–4 times higher than the minimum requirement of 9, implicating a verified SNR as specified by the DIN standard. *In vitro* tests with HeLa cells also show an analogous outcome (Fig. S7†). These results prove the shielding effect of the niosomal protective layer and thus the great potential of the synthesized hybrid niosome system to be used for analytically labelling Tf-overexpressing cancer cells such as breast carcinoma cells.

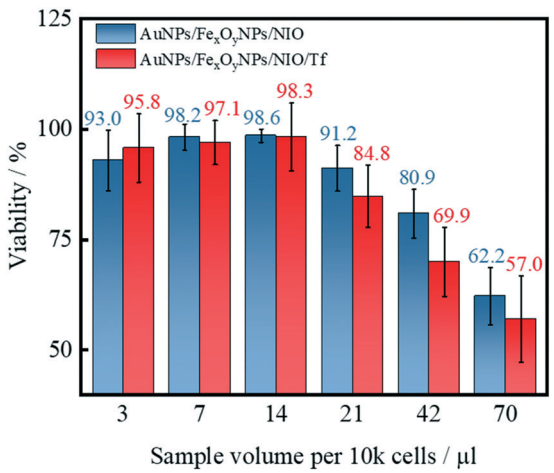

Fig. 10 Viability of MCF-7 cells after *in vitro* administration of hybrid niosomes with or without Tf-functionalization and incubation under influence of an external magnetic field.

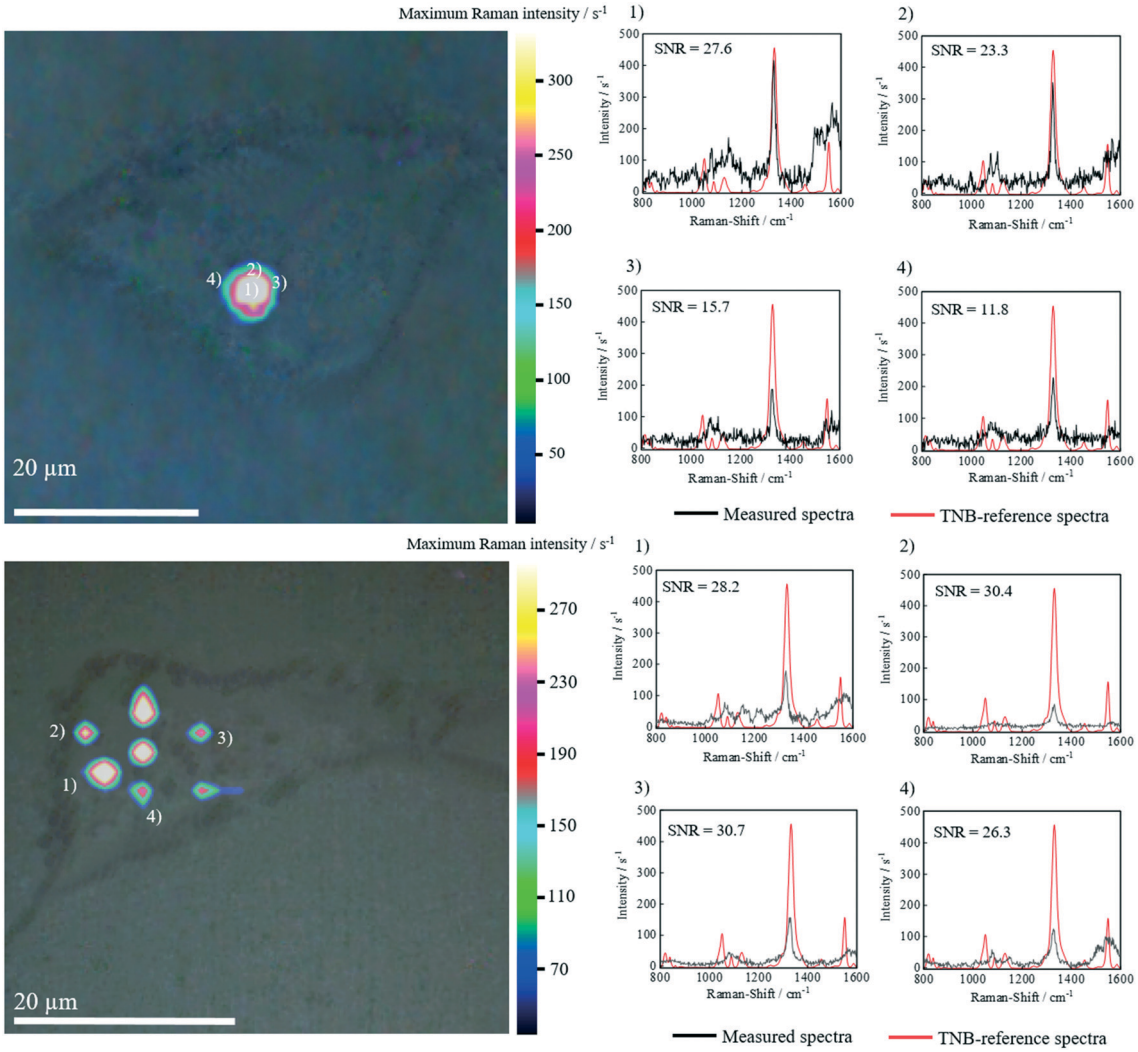

Fig. 11 (left) Merged bright field and 2D-SERS mapping images of MCF-7 cells incubated with AuNPs/Fe_xO_yNPs/NIO with the scale bars showing the maximum Raman intensities, (right) SERS-spectra and the respective signal-to-noise ratios (SNR) of the displayed 2D-SERS signals.

4. Conclusion

In this study, we presented the first successful preparation and *in vitro* application of superparamagnetic and SERS-active niosomes. The synthesized AuNPs/Fe_xO_yNPs/NIO hybrid NPs exhibited SERS-signals that could be strongly enhanced by addition of HCl to the AuNPs before encapsulation or by using a higher overall AuNP mass fraction. The entrapped Fe_xO_yNPs enabled a magnetic purification procedure and magnetic targeting using an external magnetic field. An in-depth characterization revealed the formation of highly defined hybrid structures visible in a number of representative TEM images. Furthermore, the niosome shell induced the formation of interparticle hot spots and shielded the AuNPs from multiple influences such as high salt concentrations, protein coronas, and acidic environments, affirming an extraordinary colloidal SERS-signal stability. Functionalizing the surface with Tf led to an increased Zeta potential and a slightly decreased viability of hybrid niosome-containing MCF-7 cells at specific concentrations. These observations clearly point to an enhanced internalization efficacy of hybrid niosomes due to coupling Tf onto their surface. Using the dual targeting functionality by applying an external magnetic field after *in vitro* administration of Tf-modified hybrid niosomes, their cellular uptake by the MCF-7 cells was observed. The internalized hybrid niosomes exhibited eminent SERS-signal intensities with almost no signal contamination. All measured SNR ratios indicate a successful validation of the present detection procedure according to the German standard method DIN 32645. These results confirm the initial hypothesis of utilizing niosomes to produce chemically and physically stable hybrid NPs with superparamagnetic and SERS-active properties to achieve a SERS-based monitoring of breast cancer cells, thereby bearing the potential of achieving higher sensitivity than alternative, *e.g.* fluorescence-based, detection platforms.

To validate SERS-based imaging and monitoring of tumorous tissues for *ex vivo* diagnosis or even for staining

tumor cells *in vivo* using the presented hybrid niosomes, extensive and elaborate *in vivo* experiments are mandatory. Since we chose TNB as the Raman-active compound, the hybrid niosomes possess the inherent capability to establish a quantification principle using the isotope dilution (ID) technique, which has already been used in combination with SERS.[93–95] Therefore, apart from *ex vivo* quantification procedures to investigate biomarker concentrations in human fluids (blood, cerebrospinal fluid *etc.*), an *in vivo* ID-SERS approach could aim to establish a correlation between the isotope-based Raman-shift and 2D-SERS measurements to draw conclusions about the volume and shape of the tumor. In essence, the results from this study bear great potential to establish a novel and highly sensitive imaging technique which allows monitoring and prospectively targeting of smallest cancerous breast tissues.

Author contributions

VM designed and performed the experiments, analyzed the results and wrote the manuscript. AZ, DA and CF performed further experiments and were responsible for additional data interpretation. ZW was responsible for the FDTD simulation. VM, VH, DO, SW and NW performed the experimental SERS trials. FS, RS and GG supervised the study and reviewed the manuscript. All authors approved the final manuscript.

Conflicts of interest

The authors declare no competing financial interest.

Acknowledgements

The authors thank the Laboratory of Nano and Quantum Engineering (LNQE) of the Leibniz University Hannover for use of the TEM instrument, and Bilal Temel, Institute for Particle Technology, Technische Universität Braunschweig, for carrying out the measurements.

References

1 E. R. Myers, P. Moorman, J. M. Gierisch, L. J. Havrilesky, L. J. Grimm, S. Ghate, B. Davidson, R. C. Mongtomery, M. J. Crowley, D. C. McCrory, A. Kendrick and G. D. Sanders, *JAMA, J. Am. Med. Assoc.*, 2015, **314**, 1615–1634.
2 W. H. Organization, *WHO position paper on mammography screening*, World Health Organization, Geneva, 2014.
3 R. Swaminathan, E. Lucas and R. Sankaranarayanan, *IARC Sci. Publ.*, 2011, 23–31.
4 J. Ferlay, M. Colombet, I. Soerjomataram, C. Mathers, D. M. Parkin, M. Piñeros, A. Znaor and F. Bray, *Int. J. Cancer*, 2019, **144**, 1941–1953.
5 Early Breast Cancer Trialists' Collaborative Group (EBCTCG), R. Peto, C. Davies, J. Godwin, R. Gray, H. C. Pan, M. Clarke, D. Cutter, S. Darby, P. McGale, C. Taylor, Y. C. Wang, J. Bergh, A. Di Leo, K. Albain, S. Swain, M. Piccart and K. Pritchard, *Lancet*, 2012, **379**, 432–444.
6 Early Breast Cancer Trialists' Collaborative Group (EBCTCG), *Lancet*, 2015, **386**, 1341–1352.
7 H. Pan, R. Gray, J. Braybrooke, C. Davies, C. Taylor, P. McGale, R. Peto, K. I. Pritchard, J. Bergh, M. Dowsett and D. F. Hayes, *N. Engl. J. Med.*, 2017, **377**, 1836–1846.
8 K. Kneipp, H. Kneipp, I. Itzkan, R. R. Dasari and M. S. Feld, *Chem. Rev.*, 1999, **99**, 2957–2976.
9 J. Kneipp, H. Kneipp and K. Kneipp, *Chem. Soc. Rev.*, 2008, **37**, 1052–1060.
10 J. N. Anker, W. P. Hall, O. Lyandres, N. C. Shah, J. Zhao and R. P. van Duyne, *Nat. Mater.*, 2008, **7**, 442–453.
11 S. Laing, K. Gracie and K. Faulds, *Chem. Soc. Rev.*, 2016, **45**, 1901–1918.
12 S. L. Kleinman, R. R. Frontiera, A.-I. Henry, J. A. Dieringer and R. P. van Duyne, *Phys. Chem. Chem. Phys.*, 2013, **15**, 21–36.
13 L. Fabris, *ChemNanoMat*, 2016, **2**, 249–258.
14 E. Lenzi, D. Jimenez de Aberasturi and L. M. Liz-Marzán, *ACS Sens.*, 2019, **4**, 1126–1137.
15 R. A. Rippel and A. M. Seifalian, *J. Nanosci. Nanotechnol.*, 2011, **11**, 3740–3748.
16 K. Kalimuthu, B. S. Cha, S. Kim and K. S. Park, *Microchem. J.*, 2020, **152**, 104296.
17 V. Mohammadzadeh, M. Barani, M. S. Amiri, M. E. Taghavizadeh Yazdi, M. Hassanisaadi, A. Rahdar and R. S. Varma, *Sustainable Chem. Pharm.*, 2022, **25**, 100606.
18 M. Hassanisaadi, G. H. S. Bonjar, A. Rahdar, S. Pandey, A. Hosseinipour and R. Abdolshahi, *Nanomaterials*, 2021, **11**, 2033.
19 K. Sayyadi, A. Rahdar, N. Esmaili and J. Sayyadi, *Adv. Nanochem.*, 2019, **1**, 47–51.
20 M. Mukhtar, M. Bilal, A. Rahdar, M. Barani, R. Arshad, T. Behl, C. Brisc, F. Banica and S. Bungau, *Chemosensors*, 2020, **8**, 117.
21 A. Rahdar, P. Hasanein, M. Bilal, H. Beyzaei and G. Z. Kyzas, *Life Sci.*, 2021, **276**, 119420.
22 R. Arshad, T. A. Tabish, M. H. Kiani, I. M. Ibrahim, G. Shahnaz, A. Rahdar, M. Kang and S. Pandey, *Nanomaterials*, 2021, **11**, 1086.
23 G. Bodelón, V. Montes-García, C. Fernández-López, I. Pastoriza-Santos, J. Pérez-Juste and L. M. Liz-Marzán, *Small*, 2015, **11**, 4149–4157.
24 M. S. Strozyk, D. J. de Aberasturi, J. V. Gregory, M. Brust, J. Lahann and L. M. Liz-Marzán, *Adv. Funct. Mater.*, 2017, **27**, 1701626.
25 M. S. Strozyk, D. Jimenez de Aberasturi and L. M. Liz-Marzán, *Chem. Rec.*, 2018, **18**, 807–818.
26 C. Zong, M. Xu, L.-J. Xu, T. Wei, X. Ma, X.-S. Zheng, R. Hu and B. Ren, *Chem. Rev.*, 2018, **118**, 4946–4980.
27 S. de Vitis, M. L. Coluccio, F. Gentile, N. Malara, G. Perozziello, E. Dattola, P. Candeloro and E. Di Fabrizio, *Opt. Lasers Eng.*, 2016, **76**, 9–16.
28 J. Wang, K. M. Koo, E. J. H. Wee, Y. Wang and M. Trau, *Nanoscale*, 2017, **9**, 3496–3503.
29 Y. Wang, S. Kang, A. Khan, G. Ruttner, S. Y. Leigh, M. Murray, S. Abeytunge, G. Peterson, M. Rajadhyaksha, S. Dintzis, S. Javid and J. T. C. Liu, *Sci. Rep.*, 2016, **6**, 21242.

30 V. Moisoiu, A. Socaciu, A. Stefancu, S. Iancu, I. Boros, C. Alecsa, C. Rachieriu, A. Chiorean, D. Eniu, N. Leopold, C. Socaciu and D. Eniu, *Appl. Sci.*, 2019, **9**, 806.
31 Y.-F. Huang, H.-P. Zhu, G.-K. Liu, D.-Y. Wu, B. Ren and Z.-Q. Tian, *J. Am. Chem. Soc.*, 2010, **132**, 9244–9246.
32 A. Shamsaie, M. Jonczyk, J. Sturgis, J. Paul Robinson and J. Irudayaraj, *J. Biomed. Opt.*, 2007, **12**, 20502.
33 C. D. Walkey and W. C. W. Chan, *Chem. Soc. Rev.*, 2012, **41**, 2780–2799.
34 X.-S. Zheng, I. J. Jahn, K. Weber, D. Cialla-May and J. Popp, *Spectrochim. Acta, Part A*, 2018, **197**, 56–77.
35 S. Laing, L. E. Jamieson, K. Faulds and D. Graham, *Nat. Rev. Chem.*, 2017, **1**, 501.
36 B. Pelaz, G. Charron, C. Pfeiffer, Y. Zhao, J. M. de La Fuente, X.-J. Liang, W. J. Parak and P. Del Pino, *Small*, 2013, **9**, 1573–1584.
37 J. Piella, N. G. Bastús and V. Puntes, *Bioconjugate Chem.*, 2017, **28**, 88–97.
38 N. M. S. Sirimuthu, C. D. Syme and J. M. Cooper, *Chem. Commun.*, 2011, **47**, 4099–4101.
39 Arbeitsausschuss Chemische Terminologie (AChT) im DIN Deutsches Institut für Normung e.V., DIN 32645:2008-11, Chemische Analytik_- Nachweis-, Erfassungs- und Bestimmungsgrenze unter Wiederholbedingungen_- Begriffe, Verfahren, Auswertung, Beuth Verlag GmbH, Berlin.
40 ICH Secretariat, ICH-Q2(R1) Validation of analytical procedures: Text and Methodology. International Conference on Harmonization (ICH) of Technical Requirements for the Registration of Pharmaceuticals for Human Use, Geneva, 2005.
41 Z. Zhang, L. Wang, J. Wang, X. Jiang, X. Li, Z. Hu, Y. Ji, X. Wu and C. Chen, *Adv. Mater.*, 2012, **24**, 1418–1423.
42 D. Rodríguez-Fernández, J. Langer, M. Henriksen-Lacey and L. M. Liz-Marzán, *Chem. Mater.*, 2015, **27**, 2540–2545.
43 A. F. Stewart, A. Lee, A. Ahmed, S. Ip, E. Kumacheva and G. C. Walker, *ACS Nano*, 2014, **8**, 5462–5467.
44 J. H. Kang and Y. T. Ko, *Int. J. Nanomed.*, 2015, **10**, 33–45.
45 S. Y. Ip, C. M. MacLaughlin, N. Mullaithilaga, M. Joseph, S. Wala, C. Wang and G. C. Walker, *Proc. SPIE*, 2012, **8212**, 821204.
46 U. S. Dinish, Z. Song, C. J. H. Ho, G. Balasundaram, A. B. E. Attia, X. Lu, B. Z. Tang, B. Liu and M. Olivo, *Adv. Funct. Mater.*, 2015, **25**, 2316–2325.
47 P. Verderio, S. Avvakumova, G. Alessio, M. Bellini, M. Colombo, E. Galbiati, S. Mazzucchelli, J. P. Avila, B. Santini and D. Prosperi, *Adv. Healthcare Mater.*, 2014, **3**, 957–976.
48 Y. Wang and S. Schlücker, *Analyst*, 2013, **138**, 2224–2238.
49 Y. Wang, A. B. Serrano, K. Sentosun, S. Bals and L. M. Liz-Marzán, *Small*, 2015, **11**, 4314–4320.
50 B. Khlebtsov, T. Pylaev, V. Khanadeev, D. Bratashov and N. Khlebtsov, *RSC Adv.*, 2017, **7**, 40834–40841.
51 H.-M. Kim, D.-M. Kim, C. Jeong, S. Y. Park, M. G. Cha, Y. Ha, D. Jang, S. Kyeong, X.-H. Pham, E. Hahm, S. H. Lee, D. H. Jeong, Y.-S. Lee, D.-E. Kim and B.-H. Jun, *Sci. Rep.*, 2018, **8**, 13938.
52 D. Zhu, Z. Wang, S. Zong, H. Chen, X. Wu, Y. Pei, P. Chen, X. Ma and Y. Cui, *Nanoscale*, 2014, **6**, 8155–8161.
53 G. von White, Y. Chen, J. Roder-Hanna, G. D. Bothun and C. L. Kitchens, *ACS Nano*, 2012, **6**, 4678–4685.
54 H.-Y. Lee, S. H. R. Shin, L. L. Abezgauz, S. A. Lewis, A. M. Chirsan, D. D. Danino and K. J. M. Bishop, *J. Am. Chem. Soc.*, 2013, **135**, 5950–5953.
55 J. Nam, Y. S. Ha, S. Hwang, W. Lee, J. Song, J. Yoo and S. Kim, *Nanoscale*, 2013, **5**, 10175–10178.
56 T. Lajunen, L. Viitala, L.-S. Kontturi, T. Laaksonen, H. Liang, E. Vuorimaa-Laukkanen, T. Viitala, X. Le Guével, M. Yliperttula, L. Murtomäki and A. Urtti, *J. Controlled Release*, 2015, **203**, 85–98.
57 B. Y. Moghadam, W.-C. Hou, C. Corredor, P. Westerhoff and J. D. Posner, *Langmuir*, 2012, **28**, 16318–16326.
58 E. M. Curtis, A. H. Bahrami, T. R. Weikl and C. K. Hall, *Nanoscale*, 2015, **7**, 14505–14514.
59 D. Ag Seleci, V. Maurer, F. B. Barlas, J. C. Porsiel, B. Temel, E. Ceylan, S. Timur, F. Stahl, T. Scheper and G. Garnweitner, *Int. J. Mol. Sci.*, 2021, **22**, 4556.
60 D. Ag Seleci, M. Seleci, J.-G. Walter, F. Stahl and T. Scheper, *J. Nanomater.*, 2016, **2016**, 7372306.
61 D. Ag Seleci, V. Maurer, F. Stahl, T. Scheper and G. Garnweitner, *Int. J. Mol. Sci.*, 2019, **20**, 4696.
62 S. Shilpa, B. P. Srinivasan and M. Chauhan, *Int. J. Drug Delivery*, 2011, **3**, 14–24.
63 S. Moghassemi and A. Hadjizadeh, *J. Controlled Release*, 2014, **185**, 22–36.
64 C. F. Okey-Onyesolu, M. Hassanisaadi, M. Bilal, M. Barani, A. Rahdar, J. Iqbal and G. Z. Kyzas, *ChemistrySelect*, 2021, **6**, 8645–8663.
65 C. Marianecci, L. Di Marzio, F. Rinaldi, C. Celia, D. Paolino, F. Alhaique, S. Esposito and M. Carafa, *Adv. Colloid Interface Sci.*, 2014, **205**, 187–206.
66 I. F. Uchegbu and S. P. Vyas, *Int. J. Pharm.*, 1998, **172**, 33–70.
67 D. Ag Seleci, M. Seleci, F. Stahl and T. Scheper, *RSC Adv.*, 2017, **7**, 33378–33384.
68 M. G. Arafa, D. Ghalwash, D. M. El-Kersh and M. M. Elmazar, *Sci. Rep.*, 2018, **8**, 18056.
69 I. P. Kaur, D. Aggarwal, H. Singh and S. Kakkar, *Graefes Arch. Clin. Exp. Ophthalmol.*, 2010, **248**, 1467–1472.
70 L. Seguella, F. Rinaldi, C. Marianecci, R. Capuano, M. Pesce, G. Annunziata, F. Casano, G. Bassotti, A. Sidoni, M. Milone, G. Aprea, G. D. de Palma, M. Carafa, M. Pesce, G. Esposito and G. Sarnelli, *J. Cell. Mol. Med.*, 2020, **24**, 3053–3063.
71 V. Maurer, C. Frank, J. C. Porsiel, S. Zellmer, G. Garnweitner and R. Stosch, *J. Biophotonics*, 2020, **13**, e201960090.
72 V. Maurer, S. Altin, D. Ag Seleci, A. Zarinwall, B. Temel, P. M. Vogt, S. Strauß, F. Stahl, T. Scheper, V. Bucan and G. Garnweitner, *Pharmaceutics*, 2021, **13**, 394.
73 S. Jose, T. A. Cinu, R. Sebastian, M. H. Shoja, N. A. Aleykutty, A. Durazzo, M. Lucarini, A. Santini and E. B. Souto, *Polymer*, 2019, **11**, 1905.
74 H. A. Joshi, E. S. Attar, P. Dandekar and P. V. Devarajan, in *Targeted Intracellular Drug Delivery by Receptor Mediated Endocytosis*, ed. P. V. Devarajan, P. Dandekar and A. A.

D'Souza, Springer International Publishing, Cham, 2019, pp. 457–480.
75 A. F. Oskooi, D. Roundy, M. Ibanescu, P. Bermel, J. D. Joannopoulos and S. G. Johnson, *Comput. Phys. Commun.*, 2010, **181**, 687–702.
76 C. V. Yerin, V. I. Lykhmanova and M. V. Yerina, *Magnetohydrodynamics*, 2018, **54**, 157–162.
77 P. B. Johnson and R. W. Christy, *Phys. Rev. B: Solid State*, 1972, **6**, 4370–4379.
78 S. Saavedra-Alonso, P. Zapata-Benavides, A. K. Chavez-Escamilla, E. Manilla-Muñoz, D. E. Zamora-Avila, M. A. Franco-Molina and C. Rodriguez-Padilla, *Exp. Ther. Med.*, 2016, **12**, 3778–3784.
79 American Society for Testing and Materials, E1840-96, *Standard guide for Raman shift standards for spectrometer calibration*, 2007.
80 D. S. Grubisha, R. J. Lipert, H.-Y. Park, J. Driskell and M. D. Porter, *Anal. Chem.*, 2003, **75**, 5936–5943.
81 P.-P. Fang, J.-F. Li, Z.-L. Yang, L.-M. Li, B. Ren and Z.-Q. Tian, *J. Raman Spectrosc.*, 2008, **39**, 1679–1687.
82 D. Zhu, Z. Wang, S. Zong, Y. Zhang, C. Chen, R. Zhang, B. Yun and Y. Cui, *Theranostics*, 2018, **8**, 941–954.
83 C. Kojima, Y. Hirano, E. Yuba, A. Harada and K. Kono, *Colloids Surf., B*, 2008, **66**, 246–252.
84 J. Rejman, V. Oberle, I. S. Zuhorn and D. Hoekstra, *Biochem. J.*, 2004, **377**, 159–169.
85 D. Drescher and J. Kneipp, *Chem. Soc. Rev.*, 2012, **41**, 5780–5799.
86 H. Hillaireau and P. Couvreur, *Cell. Mol. Life Sci.*, 2009, **66**, 2873–2896.
87 Y. Shen, X. Li, D. Dong, B. Zhang, Y. Xue and P. Shang, *Am. J. Cancer Res.*, 2018, **8**, 916–931.
88 S. Pizzamiglio, M. de Bortoli, E. Taverna, M. Signore, S. Veneroni, W. C.-S. Cho, R. Orlandi, P. Verderio and I. Bongarzone, *Int. J. Mol. Sci.*, 2017, **18**, 410.
89 H. O. Habashy, D. G. Powe, C. M. Staka, E. A. Rakha, G. Ball, A. R. Green, M. Aleskandarany, E. C. Paish, R. Douglas Macmillan, R. I. Nicholson, I. O. Ellis and J. M. W. Gee, *Breast Cancer Res. Treat.*, 2010, **119**, 283–293.
90 W. Wang, Z. Deng, H. Hatcher, L. D. Miller, X. Di, L. Tesfay, G. Sui, R. B. D'Agostino, F. M. Torti and S. V. Torti, *Cancer Res.*, 2014, **74**, 497–507.
91 A. Zarinwall, M. Asadian-Birjand, D. A. Seleci, V. Maurer, A. Trautner, G. Garnweitner and H. Fuchs, *Nanomaterials*, 2021, **11**, 1057.
92 M. Nag, V. Gajbhiye, P. Kesharwani and N. K. Jain, *Colloids Surf., B*, 2016, **148**, 363–370.
93 S. Zakel, S. Wundrack, G. O'Connor, B. Güttler and R. Stosch, *J. Raman Spectrosc.*, 2013, **44**, 1246–1252.
94 C. Frank, C. Brauckmann, M. Palos, C. G. Arsene, J. Neukammer, M. E. Del Castillo Busto, S. Zakel, C. Swart, B. Güttler and R. Stosch, *Anal. Bioanal. Chem.*, 2017, **409**, 2341–2351.
95 C. Frank, O. Rienitz, R. Jährling, D. Schiel and S. Zakel, *Metallomics*, 2012, **4**, 1239–1244.